Detection of near-surface hydrocarbon seeps using P- and S-wave reflections

Mathieu J. Duchesne[1], André J.-M. Pugin[2], Gabriel Fabien-Ouellet[3], and Mathieu Sauvageau[4]

Abstract

The combined use of P- and S-wave seismic reflection data is appealing for providing insights into active petroleum systems because P-waves are sensitive to fluids and S-waves are not. The method presented herein relies on the simultaneous acquisition of P- and S-wave data using a vibratory source operated in the inline horizontal mode. The combined analysis of P- and S-wave reflections is tested on two potential hydrocarbon seeps located in a prospective area of the St. Lawrence Lowlands in Eastern Canada. For both sites, P-wave data indicate local changes in the reflection amplitude and slow velocities, whereas S-wave data present an anomalous amplitude at one site. Differences between P- and S-wave reflection morphology and amplitude and the abrupt decrease in P-velocity are indirect lines of evidence for hydrocarbon migration toward the surface through unconsolidated sediments. Surface-gas analysis made on samples taken at one potential seeping site reveals the occurrence of thermogenic gas that presumably vents from the underlying fractured Utica Shale forming the top of the bedrock. The 3C shear data suggest that fluid migration locally disturbs the elastic properties of the matrix. The comparative analysis of P- and S-wave data along with 3C recordings makes this method not only attractive for the remote detection of shallow hydrocarbons but also for the exploration of how fluid migration impacts unconsolidated geologic media.

Introduction

Compressional (P-wave) reflections have been used since the late 1920s to image the internal structure of the subsurface, whereas shear (S-wave) reflections have only started to be used routinely at the beginning of the 1980s (McCormack et al., 1984; Sheriff and Geldart, 1995). By the early 1970s, P-wave seismic reflections started to be used to detect hydrocarbon accumulations in geologic media because they tend to produce abrupt and local changes in amplitude (Larner et al., 1974). Taner et al. (1979) propose the complex representation of real seismic traces to derive instantaneous attributes (i.e., the amplitude of the envelope or reflection strength, phase, and frequency) so lateral changes of reflection characteristics are better localized. It is the emergence of complex trace analysis with the advent of more powerful computing facilities that paved the way to a more in-depth use of seismic data and the proliferation of seismic attributes to identify hydrocarbons (Chopra and Marfurt, 2007). Still, P-wave seismic amplitude remains the chief characteristic to find hydrocarbons (Simm and Bacon, 2014).

Despite hardware breakthrough made by the Conoco Shear-Wave Group Shoot using horizontal S-wave (SH) vibrators during the late 1970s (Ensley, 1984) and followed by the azimuthal isotropic impact source of ARCO, the SH-wave Bolt airgun, and SH-wave weight drop of the Institut Français du Pétrole in the 1980s, hydrocarbon exploration using pure S-waves is still marginal and mostly a research topic (Gaiser and Strudley, 2005). Two main reasons are cited to explain the reluctance to conduct exploration surveys with S-wave sources: (1) it is challenging to produce good quality data and (2) during the 1990s, converted-wave seismology clearly demonstrated that P-wave sources are very efficient to generate S-waves (Stewart et al., 2002; Hardage and Wagner, 2014a). Nowadays, S-wave reflections are mainly used to characterize fracture networks and to image geologic media through gas clouds that frequently obscure P-wave reflections on offshore data (Dai et al., 2007). Beside exploration seismology, S-wave sources have been extensively used since the early 1990s in near-surface imaging. They are now of common use to image the shallow subsurface in hydrogeological, geotechnical,

[1]Geological Survey of Canada, Quebec City, Canada. E-mail: mathieuj.duchesne@canada.ca.
[2]Geological Survey of Canada, Ottawa, Canada. E-mail: andre.pugin@canada.ca.
[3]Institut National de la Recherche Scientifique, Centre Eau-Terre-Environnement, Quebec City, Canada. E-mail: gabriel.fabien-ouellet@ete.inrs.ca.
[4]McGill University, Department of Mining and Materials Engineering, Montreal, Canada. E-mail: mathieu.sauvageau@mail.mcgill.ca.

Manuscript received by the Editor 2 November 2015; revised manuscript received 27 March 2016; published online 14 July 2016. This paper appears in *Interpretation*, Vol. 4, No. 3 (August 2016); p. SH21–SH37, 16 FIGS., 2 TABLES.
http://dx.doi.org/10.1190/INT-2015-0175.1.

and environmental studies as they provide higher resolution than P-waves because of the slow velocity of S-waves in unconsolidated sediments (Woolery et al., 1993; Clark et al., 1994; Dasios et al., 1999; Ghose and Goudswaard, 2004; Pugin et al., 2009).

The combined use of P- and S-wave reflections is appealing because both types of wave depend on different elastic properties and are thus complementary. Hence, P-waves are sensitive to fluids because of their compressible nature (Batzle and Wang, 1992). Conversely, S-waves are not sensitive to the fluid content of geologic media because (1) fluids do not support shear stress and (2) with their direction of vibration being transverse, they do not involve the bulk modulus.

Direct hydrocarbon detection using comparative P- and S-wave seismic sections was initially introduced at the beginning of the 1980s. Ensley (1984) first suggests that the comparison of P- and S-waves seismic data could help to discriminate gas-related anomalies and those related to lithology, whereas Robertson and Pritchett (1985) apply a similar approach to remotely detect a gas-prone sandstone reservoir. Data discussed in both contributions resulted from the Conoco Shear-Wave Group Shoot experiment, and thus they are related to coincident but separated P- and S-wave acquisition. In the early 2000s, a 3D multicomponent experiment conducted by van der Kolk et al. (2001) showed that for vertical gas-filled fractures, S-wave velocity V_S decreases perpendicular to the fracture orientation because of the polarization induced by S-wave splitting, whereas P-wave velocity V_P remains unaffected (Crampin, 1985). They suggest that S-wave data should be used along with P-wave data as a direct hydrocarbon indicator over fractured reservoirs. More recently, Xue et al. (2013) use seismic attenuation of P- and S-waves to discriminate water-filled from gas-filled sandstones. They reveal that P-attenuation is larger than S-attenuation for gas-filled reservoirs, but conversely S-attenuation is greater than P-attenuation for water-filled reservoirs. Even if the number of reports on the joint use of P- and S-wave reflections surveys has increased in scientific journals, the literature still lacks of examples discussing the remote detection of hydrocarbons using the complementary information provided by P- and S-wave seismic data for shallow (<200 m) unconsolidated media. This is partly due to (1) heavy land use and restricted terrain access are making acquisition conditions difficult or virtually impossible onshore, (2) S-wave sources are problematic and expensive to operate offshore, and (3) because the oil and gas industry has little interest in near-surface imaging (Vanneste et al., 2011).

Typically, the remote detection of hydrocarbons combining P- and S-wave reflections is done using converted wave or coincident but distinct P- and S-wave seismic acquisitions over deep (>1500 m) hydrocarbon prospects. To the knowledge of the authors, comparative P- and S-wave seismic data analysis to detect near-surface hydrocarbon seeps in unconsolidated geologic media has never been presented in the literature. In the following pages, a case in which P- and S-wave data have been collected simultaneously to detect shallow (<110 m) hydrocarbon indicators in a prospective area of Eastern Canada is presented and discussed. In this paper, the following nomenclature is used to discuss wave type versus source and 3C receivers orientation: S- or P-wave (source orientation and receiver orientation). For instance, S(H1,V) means that S-waves are processed for a source operated in line horizontal and for signals recorded with vertical geophones. The acquisition was made with a vibratory source operated in the inline horizontal (S(H1)) mode and 3C receivers. The paper is an extension of preliminary results reported in Duchesne and Pugin (2014) as radiation patterns, 3C observations, and surface-gas analyses are included herein. First, theoretical and practical considerations on the simultaneous generation of P- and S-waves from S(H1) vibrations are presented. Then, acquisition and processing methods and parameters are briefly described. Next, results obtained from comparative P- and 3C S-waves analysis are detailed. Finally, correlations between seismic data and surface-gas sampling are discussed before the overall performance of the approach and the role of fluid migration on seismic anisotropy and polarization are briefly addressed and assessed.

Generating P-waves from an S(H1) vibratory source

Some studies have shown that P- and S-waves reflections can be produced using the same source (Gaiser and Strudley, 2005; Hardage and Wagner, 2014a, 2014b). These studies revealed that S(H1) and vertical (V) sources can produce usable S- and P-waves, even though the quality of the result varies greatly between sites.

From a theoretical point of view, the generation of S- and P-waves by a force applied on the free surface of a half-space has been understood for a long time. In his historical paper, Lamb (1904) describes different propagation modes created by a shock applied on a free surface, which include shear and compressional body waves. Of interest to exploration geophysics are the work of Miller and Pursey (1954) and Cherry (1962) which, respectively, give the radiation patterns for vertical and horizontal point forces along a free surface. Those patterns are far from simple because (1) phase and amplitude vary with angle and (2) P- to S-wave amplitude ratio is strongly influenced by Poisson's ratio.

Figure 1 shows radiation patterns obtained using equations 29, 30, and 31 of Cherry (1962), which correspondingly describe P(H1), S(V), and S(H1) radiation patterns for a horizontal point force parallel to the free surface of an elastic half-space. Seismic velocities used to generate radiation patterns are 350 m/s for P-waves and 200 m/s for S-waves, which are typical values for the first meters of nonsaturated soils in the survey area discussed herein. The S(H1) pattern for those values

shows P- and S-waves, although amplitudes for S-waves are much stronger (Figure 1a). Amplitudes also strongly vary with angle; i.e., S-waves are absent at angles smaller than approximately 60, and P-waves have negligible amplitudes at large angles (Figure 1b). In comparison, S(H2) sources do not produce any P-waves (Figure 1c). In general, S(H1) and S(V) sources have radiation patterns with much stronger amplitudes for S-waves than for P-waves (Figure 1d).

However, observed amplitude ratios in the field are generally much smaller than on this figure as a consequence of the oversimplification of the problem by the modeling exercise (Maercklin and Zollo, 2009). In fact, using a homogeneous half-space to approximate the near surface is idealistic because the first meters of the subsurface generally exhibit strong vertical P-wave velocity variations and frequent lateral variations for P- and S-waves velocities. Those variations are one of the reasons why field studies show highly variable quality of P- and S-wave reflections for S(H) and S(V) sources. Furthermore, approximating S(H) and S(V) sources as pure horizontally and vertically oriented forces is dubious at best. In reality, sources produce complex vibrational modes. Still, the radiation patterns for homogeneous half-spaces are very useful because they show the physical validity of producing P-waves with S(H1) sources and illustrate the complex angular amplitude and phase variations for such sources even for the simplest cases. Complex vibrational modes of S-wave sources are reported in Pugin et al. (2009) using a 9C data set. They show that P-wave sections can be processed using the vertical component of the receivers even when the source is vibrating inline and even crossline, despite the theory predicts no P-wave when a source is vibrating crossline.

Geologic setting

Data were acquired in the St. Lawrence Lowlands near Pointe-du-Lac (Eastern Canada), in which approximately 90 m thick Quaternary succession overlies the fractured, organic-rich, and gas-prone Middle Ordovician Utica Shale (Lavoie et al., 2009). Since the Middle Pleistocene, this area has successively witnessed ice sheet invasion and glacial lakes and sea flooding. The complex interplays between glacial advances and retreats and subsequent flooding episodes led to the deposition of sedimentary pile formed by glacial, deltaic, fluvial, lacustrine, and marine facies (Lamothe, 1989). According to confidential borehole logging, the site of acquisition mainly consists of thick distal and proximal marine clays deposited during the Champlain Sea episode (13,000–10,000 years) that are overlain by a coarse alluvium layer. Local occurrence of erosion-resistant till patches is probable at the base of the succession. A more complete succession is observed only a few km east of the site of study (Figure 2). This means that the area underwent at least one episode of drastic local erosion. In the surveyed area, the aquifer is confined within the bedrock or till patches just above it, whereas the Champlain Sea clays form an effective aquitard (Leblanc et al., 2013).

The region of Pointe-du-Lac is also known for the occurrence of shallow gas accumulation and seeps (St-Antoine and Héroux, 1993; Pugin et al., 2013a). The seismic line discussed below was shot a few km west of a depleted conventional gas reservoir hosted in unconsolidated and very porous (up to 36%) middle Pleistocene sand that is now intermittently used for gas storage (Intragaz, 2009). The reservoir unconformably sits on the top of the Utica Shale and is sealed by a 60–90 m thick impermeable clay layer (Lavoie et al., 2009).

Methods

Seismic data acquisition

P- and S-wave reflections were generated simultaneously on a paved road with an IVI Minivib vibrating source. The 140 kg mass was operated in the S(H1) mode using a 7 s long linear sweep from 20 to 240 Hz. Reflections were recorded with a 72 m long landstreamer developed by the Near-Surface Geophysics Section of the Geological Survey of Canada that included 48 3C (V, H1, and H2) geophone stations mounted on 3 kg metal sleds (Pugin et al., 2009). Shotpoint spacing was 4.5 m, whereas recording units were spaced 1.5 m apart, giving a fold of eight. Vertical resolution of the data sets

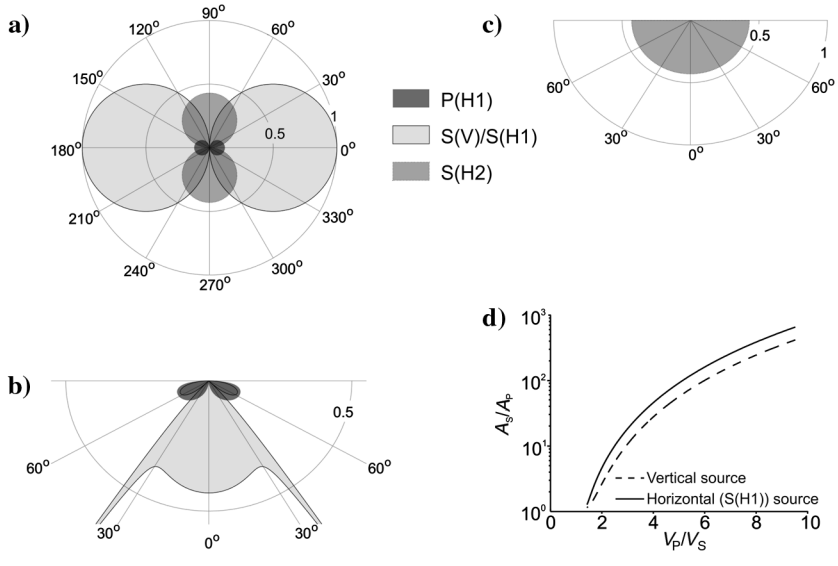

Figure 1. Radiation patterns for horizontal surface stresses distributed over the radius of an elastic half-space. (a) Plan and cross section views for a (b) S(H1) (inline) source and (c) S(H2) (crossline) surface source. (b and c) Both have a 0–180° orientation. (d) Horizontal (S(H1)) and vertical sources (P(V)) S/P amplitude ratio for different V_P/V_S ratios.

is approximately 2.6 and 1 m for P- and S-wave data, respectively. Figure 3 shows a typical shot gather recorded in the surveyed area. All 3C contain P-wave, S-wave, and surface-wave arrivals. In addition, nongeometric and converted-wave arrivals were captured by H1 and H2 receiver components.

Seismic data processing

Initial processing steps included wave mode and receiver component separation as well as geometry editing. Nonlinear vibroseis whitening deconvolution was performed in the uncorrelated domain to attenuate high-amplitude surface waves that were plaguing reflections using the method of Coruh and Costain (1983). Then, principal component decomposition by means of the Karhunen-Loéve transform was applied to remove random noise on P-waves and 3C S-waves data sets (Jones and Levy, 1987). For P-wave data, prestack spiking deconvolution was used to compress ringing effect induced by large reflection coefficients present within the near surface. Finally, P- and S-wave reflections were processed separately using the same workflow that included trace amplitude normalization, muting, velocity analysis, normal moveout (NMO) corrections, and stacking. Frequency content of the final stacks ranges from 70 to 240 and 25 to 200 Hz for P-wave and S-wave sections, respectively.

Removal of nongeometric wave and converted-wave arrivals

Additional processing was necessary to remove nongeometric-wave and converted-wave arrivals. Accord-

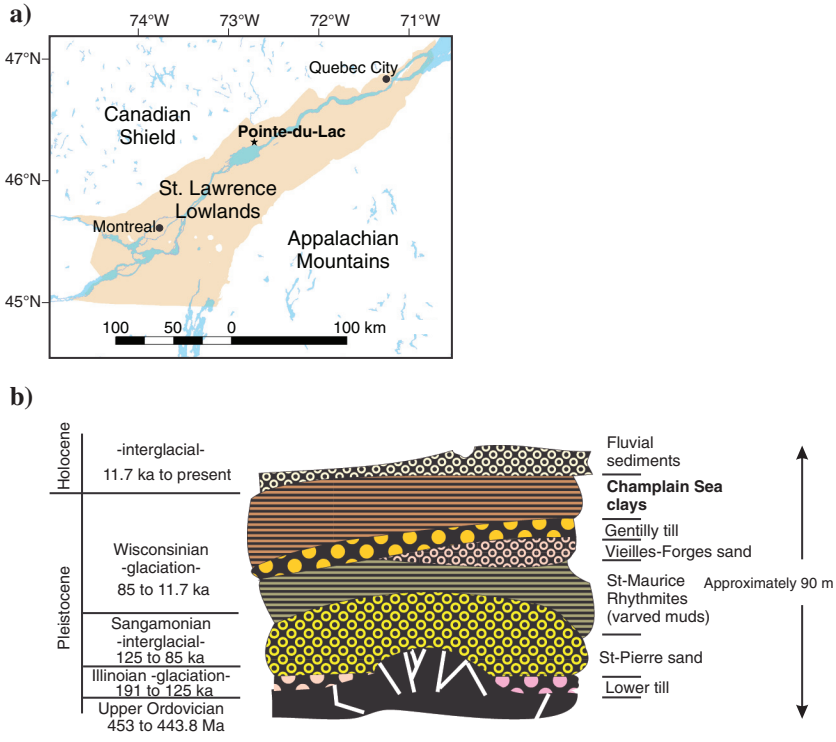

Figure 2. (a) Location map of the Pointe-du-Lac survey site and (b) stratigraphic setting for the Pointe-du-Lac area. Champlain Sea clays (in bold) are the main Quaternary stratigraphic unit observed at the site of study (modified from Lavoie et al., 2009).

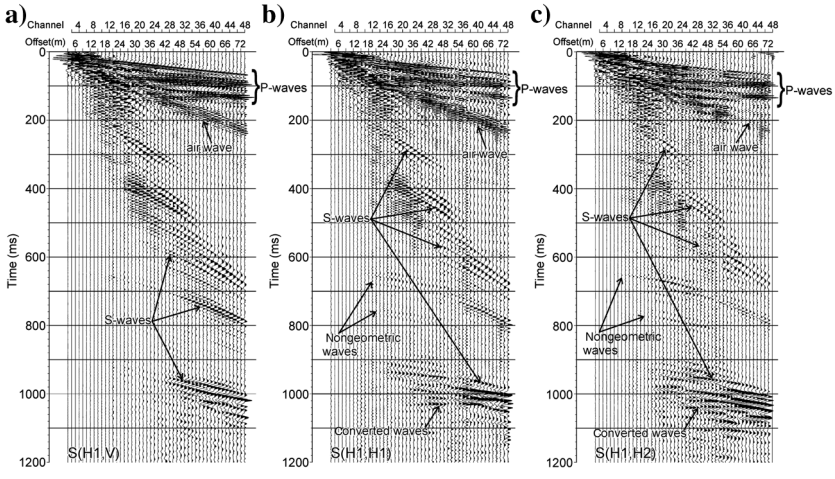

Figure 3. A typical shot gather over the surveyed area for (a) the vertical (V) component, (b) the inline (H1) component, and (c) the crossline (H2) component of the receiving system with the different arrivals annotated. Note the presence of an S-wave arrival just greater than 1000 ms on the H2-receiver component that is caused by a change in polarization.

ing to Roth and Holliger (2000) and Gao et al. (2014), nongeometric waves have the following characteristics: (1) they are linked to complex incidence angles and therefore cannot be related to any geometric raypath, (2) they tend to develop within materials having a high Poisson's ratio, (3) on shot gathers they appear on near- to mid-offset ranges, and (4) their velocity can be upward of twice the velocity of S-waves. Here, nongeometric waves are observed on shot gathers between 0 and 51 m offset, from the top of the distal marine clays (approximately 640 ms) to the top of bedrock (approximately 940 ms) in which Poisson's ratio ranges from 0.46 to 0.48. Observed velocities range between 230 and 250 m/s, which is approximately 1.5 times faster than what is expected within the surveyed area. Nongeometric wave arrivals appear to be better recorded on the horizontal components (H1-H2) of the receiver stations. Converted-wave arrivals were also recorded on the far offsets and possess very little moveout. Because nongeometric and converted-wave arrivals are coherent as S(H1,H1-H2) wave arrivals, they will impede all processing steps relying on coherence such as semblance analysis that is conventionally used to determine NMO corrections. Fortunately, several methods exist to remove or attenuate coherent noise on seismic data. These methods are typically applied in the time-distance (t-x), time of intercept slope (Tau-P), or frequency-wavenumber (f-k) domains. However, depending on data set characteristics such as fold and spatial or frequency aliasing, the removal of nongeometric and converted waves is restricted to certain domains. Moreover, for 2D near-surface data, drastic lateral changes in dips of coherent noise, statics, and amplitude are typically observed (Wiest and Edelmann, 1984; Taylor et al., 2014). Because of that, τ-p and f-k approaches tend to severely smear the noise and damage the data. Because data sets used in this study were spatially aliased and suffered from large lateral amplitude variations induced by complex near-surface conditions, the t-x domain was chosen to remove nongeometric and converted waves. The method used is inspired by the one presented in Chiu and Butler (1997). Coherent noise representing nongeometric and converted-wave arrivals is modeled along selected dips defined by their NMO velocities. Dips are computed by using the envelope of the wavelets, hence energy is maximized to avoid dip aliasing that could be introduced in the solution by selecting dips that belong to neighboring wavetrains. Afterward, noise wavelets are constructed along those dips by including all frequencies covering the bandwidth of nongeometric and converted waves. Each dip is processed separately so the constructed noise wavelets are not smeared by large dip variations. By doing so, the original waveform is preserved or minimally distorted after coherent noise removal. Then, modeled wavelets are matched for statics and amplitude with their corresponding trace on the common midpoint (CMP) gather so wavelets remain sharp and not smeared by statics jumps or noise curvature before being adaptively subtracted from the original CMP gathers. Figure 4 presents an example of the removal of nongeometric and converted-wave arrivals on an H1-receiver component CMP gather. The difference plot shows that much of the nongeometric and converted-wave energy has been successfully removed from the data with only a minimum of S-wave energy being cut out along the way (Figure 4c). Figure 4d indicates that the method has not affected the original bandwidth of the data because only amplitudes of the frequencies between 38 and 84 Hz, i.e., the bandwidth over which nongeometric and converted-wave arrivals were contained, have been trimmed down, whereas the original amplitude decay toward high frequencies has

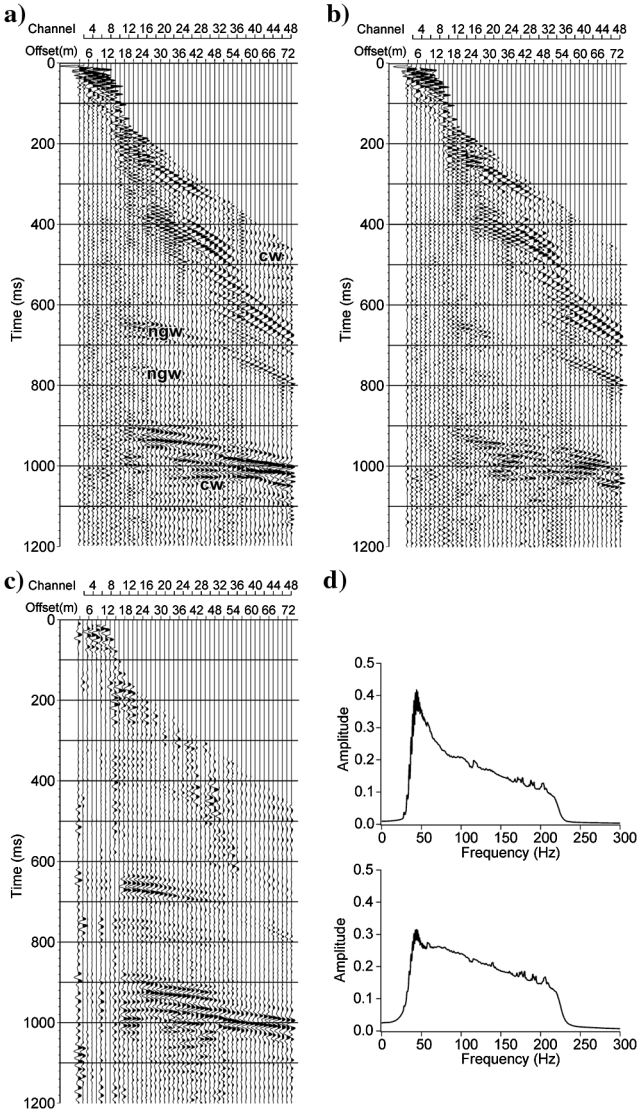

Figure 4. Removal of nongeometric and converted-wave arrivals. (a) S(H1,H1) shot gather muted for P- and air-wave arrivals (cw, converted waves; ngw, nongeometric waves), (b) shot gather shown in (a) after the removal of nongeometric and converted-wave arrivals, (c) difference plot of (a and b), and (d) amplitude spectra of (a) (top) and (b) (bottom).

been preserved. Figure 5 shows semblance plots of a H1-receiver component CMP gather before and after the removal of nongeometric wave arrivals. This figure not only demonstrates the effectiveness of the filter but also that nongeometric events can easily lead to erroneous velocity picks that can echo into the following steps of the processing flow and ultimately falsify subsurface imaging.

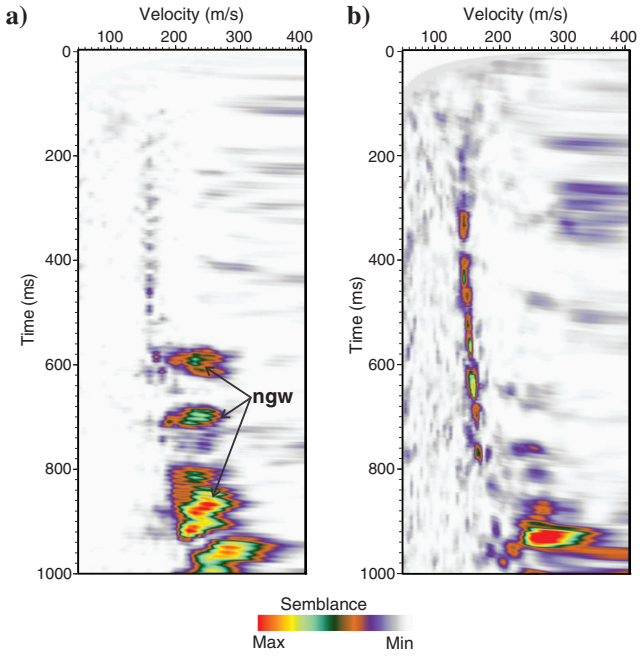

Figure 5. Semblance-based S-wave velocity analyses made on a CMP for receiver component H1 (a) before and (b) after the removal of nongeometric wave (ngw) arrivals.

Surface-gas sampling

Surface-gas sampling was conducted at site 2 where fluids are suspected to vent at the free surface based on anomalous P(H1,V) seismic features observed at this location (Figure 6). Sampling stations were positioned with 17 m spacing over a 595 m long stretch using shotpoint locations. The sampling probe was inserted at 1.5 m below the surface. Gases were collected using an air-tight syringe before being processed by a laboratory where they were identified and quantified by chromatography.

Results

Seismic stratigraphic interpretation

Figure 6 shows key seismic stratigraphic markers as imaged by P- and S-wave reflections. The S-wave section was generated by first vertically stacking all three receiver components together in the shot domain before performing a CMP stack. This allows capturing the maximum of the reflected energy induced by changes of polarization with depth. These changes are most likely related to variations in elastic properties correlative to geologic layers. The result is an image that can document as much as possible the stratigraphic architecture of the subsurface with the highest signal-to-noise ratio achievable.

Stratigraphic markers were tied to reflections using confidential well-log data collected in two boreholes intersecting the seismic line (Figure 6). Overall, the

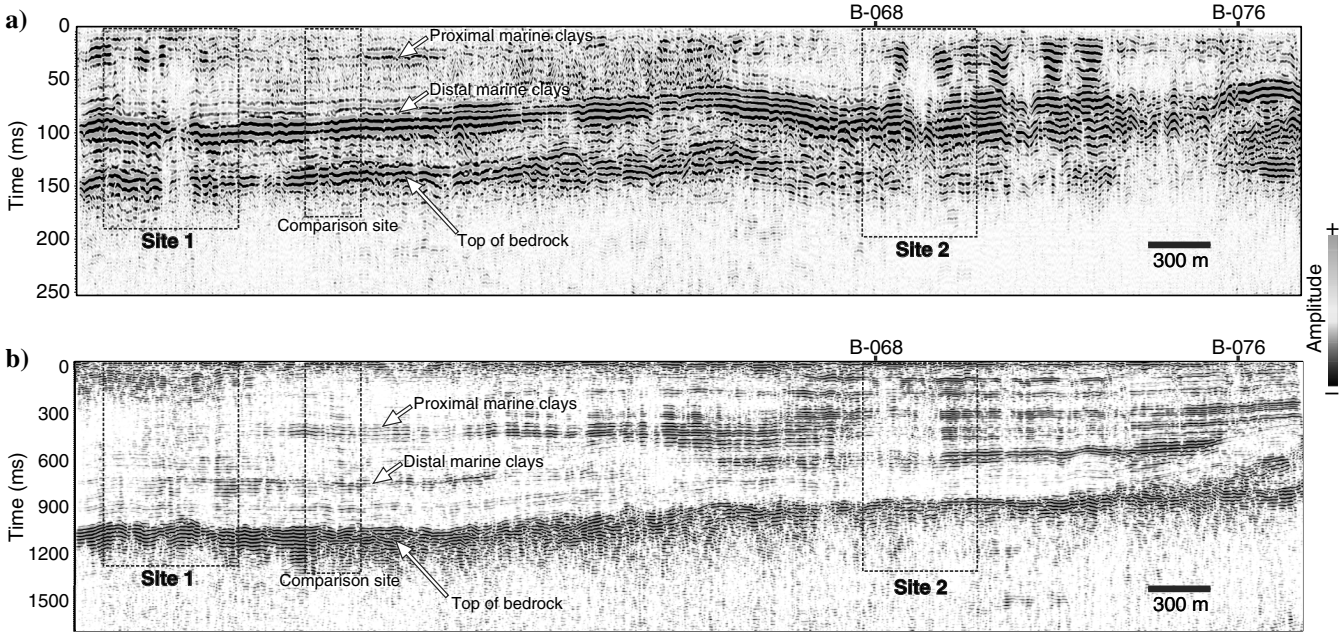

Figure 6. (a) P-wave section and (b) 3C stack S-wave section showing key seismic stratigraphic markers. The dashed line boxes show location of the sites 1 and 2 discussed in the paper. Boreholes B-068 and B076 used for geologic correlations are located at the surface.

S-wave section provides much more resolution then the P-wave section thanks to slower S-wave velocities. On P- and S-wave sections, the top of bedrock corresponds to rocks of the Utica Shale (Lavoie et al., 2009). On both sections, the reflection is flat to slightly undulated and of high amplitude. Bedrock was encountered at 89 and 92 m in boreholes B-068 and B-076, respectively (Figure 6). Sometimes local occurrences of till patches can be mistaken for the top of the bedrock reflection as the contact between the till and overlying distal marine clays presents an acoustic impedance contrast that is larger than the one between the top of the bedrock and the till. On the P-wave section, the top of the highly compacted distal marine clays appears as a strong amplitude reflection that mimics the morphology of the bedrock. This is most probably the result of a tuning effect produced by unresolved alternating thin layers of clay, silt, and sand forming the summit of this succession (Clet and Occhietti, 1996). On the S-wave section, the same marker shows great changes in amplitude but possesses the same draping morphology as its P-wave equivalent. Just below, thin strata interfaces that are unresolved on the P-wave section appear as a faint parallel layering (Figure 6). The top of the P- and S-wave sections consists of reflections attributed to proximal marine clays that are less compacted than their distal counterpart. In the next section, two zones interpreted as potential near-surface hydrocarbon indicators, identified as sites 1 and 2 in Figure 6 are discussed.

P- and S-wave time-amplitude observations made on potential hydrocarbon indicators

Site 1 is characterized by a blanked zone on the P-wave section in which amplitudes are abruptly diminished at the reflection delimiting the bedrock from the unconsolidated sediments. However, on the S-wave section, the reflection that marks the top of the bedrock maintains a bright character (Figure 6). Figure 7 presents P(H1,V), S(H1,V), S(H1,H1), and S(H1,H2) sections at site 1. None of the S-wave components show the noticeable change of amplitude observed on the P-wave section. Interestingly enough are the high-amplitude reflections recorded by the H2-receiver component between the top of the bedrock marker and approximately 725 ms.

Site 2 is part of an area where P-wave amplitudes are anomalous (Figure 8). This site shows a blanked zone bordered by two high-amplitude pull-down reflection packages on the P(H1,V) section that are not apparent on any of the S-wave sections. S-wave reflections located above the bedrock reflection stay mostly flat and a vertically disturbed zone is sharply bordered by bright reflections (Figure 6). At site 2, P(H1,V) the data show anomalous times and amplitudes, whereas S-wave data only present anomalous amplitudes (Figure 8). As it is the case for site 1, the H2-receiver component presents high-amplitude reflections sitting on the top of the bedrock reflection. This time however the shallowest of those reflections corresponds to the top of the distal marine clays, which is not the case at site 1. On the S(H1,V) and S(H1,H1) sections, reflected energy is only recorded at the top of the distal marine clays. Above the top of the distal marine clays, higher amplitudes are captured by the V-receiver component but the general reflection character, i.e., a vertically disturbed zone bordered, respectively, on the left and the right by low- and high-amplitude reflections, remains the same for the 3C.

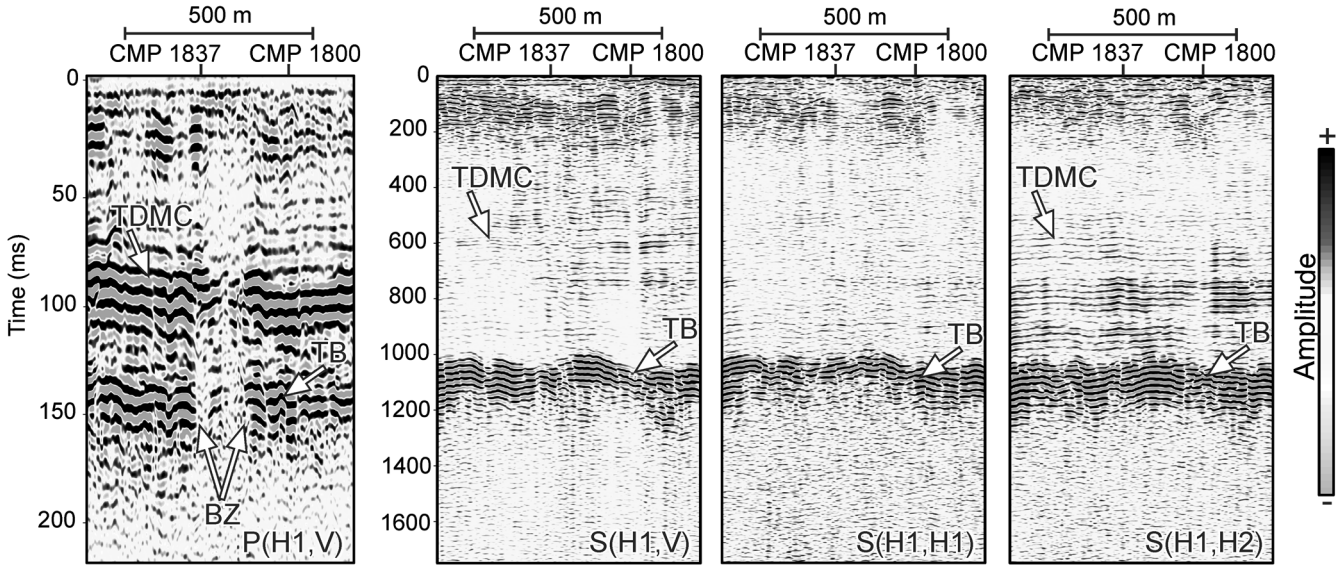

Figure 7. P(H1,V), S(H1,V), S(H1,H1), and S(H1,H2) sections at site 1. TDMC, top of distal marine clays; TB, top of bedrock; and BZ, blanked zone. CMPs used for velocity analyses shown in Figures 8 and 9 are indicated at the top of the sections. See Figure 6 for site 1 location.

P-wave and 3C S-wave velocity analyses

Semblance-based P-wave velocity analyses are shown in Figure 9. For comparison purposes, analyses that have been conducted on CMPs located within and outside the suspected hydrocarbon indicators are presented. At both sites, P-waves are slower within the blanked zone and the pulled-down high-amplitude reflection package than next to these features. At site 1, the top of the bedrock reflection at CMP 1837 reveals a velocity of 1685 m/s within the blanked zone, whereas at CMP 1800, i.e., approximately 235 m right of this zone, the velocity increases to 1878 m/s. For the top of the distal marine clays marker, velocity is 1262 and 1570 m/s inside and outside the seismically perturbed region correspondingly. At site 2, within the high-amplitude pulled-down reflections package at CMP 630, the top of the bedrock reflection has a velocity of 1306 m/s as opposed to 1745 m/s at CMP 535 positioned 250 m on its right. Above, the reflection correlative to the top of the distal marine clays has a velocity of 1143 m/s within the anomalous zone (CMP 630) versus 1460 m/s outside this same zone (CMP 535).

Figure 10 shows semblance velocity picks made on CMPs discussed above at both sites for P(H1,V) and S (H1,V) data sets. Velocities were picked using maximum semblance. For sites 1 and 2, contrasting velocity plots are pictured by S(H1,V) picks selected inside and outside the anomalous regions. Conversely, S(H1,V) velocities picked within and next to both anomalous amplitude locations imaged on the P(H1,V) seismic section remain similar.

The 3C semblance-based S-wave velocity analyses computed for sites 1 and 2 are presented in Figure 11. For all 3C, the average semblance has been calculated using all CMPs that covered each site; i.e., 213 and 200 CMPs at sites 1 and 2, respectively. This was done to capture the site specific trend of velocity changes over time for vertical, inline, and crossline components. In general, lower semblance values are measured over site 1 as opposed to site 2. S(H1,H1) and S(H1,H2) semblance plots of site 1 also show a noisier appearance than those computed for the same components on site 2. These two characteristics are presumably inherited from the lower amplitude events recorded at site 1 (Figures 7, 8, and 11). However, for both sites there is a clear decrease in semblance at the top of the distal marine clay marker at approximately 600 ms on the H1-receiver component, although the overall trend can still be followed from this marker down to the bedrock interface at site 2. Contrastingly, the time interval between those two markers presents much higher semblance values on the H2-receiver component. Figure 12 displays S(H1,V), S(H1,H1), and S(H1,H2) semblance-based velocity picks selected at sites 1 and 2. Velocities were picked automatically using maximum semblance values as much as possible except on the H2-receiver component for both sites where manual picks were selected to avoid the selection of suspect high semblances attributed to residual nongeometric wave arrivals observed between the top of the bedrock and the top of the distal marine clay events. At sites 1 and 2, velocity of all 3C follows the same trend; i.e., velocity slowly increases with time before abruptly rising at the top of the bedrock. Additional semblance analyses have been conducted between CMPs 1550 and 1650, a portion of the seismic line free of anomalous amplitude and time on the P(H1,V) section (Figures 6, 13, and 14; Table 1). For all 3C, the average velocity of the unconsolidated sediment succession is comparable with those CMPs. However, velocities are slightly and considerably slower

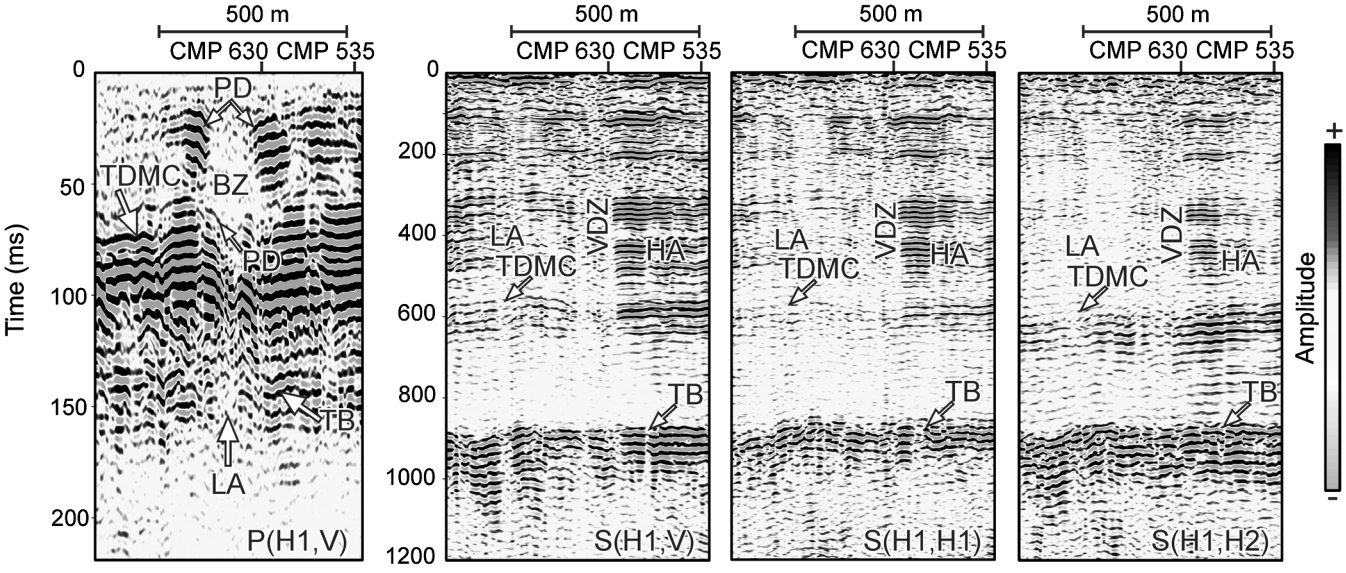

Figure 8. P(H1,V), S(H1,V), S(H1,H1), and S(H1,H2) sections at site 2. TDMC, top of distal marine clays; TB, top of bedrock; BZ, blanked zone; PD, pull-down; LA, low amplitude; HA, high amplitude; and VDZ, vertically disturbed zone. CMPs used for velocity analyses shown in Figures 8 and 9 are indicated at the top of the sections. See Figure 6 for location.

than what is observed at sites 1 and 2, respectively. Table 1 summarizes average 3C S-wave velocities computed from semblance picks made on every CMP covering sites 1 and 2.

Surface-gas analysis and correlation with seismic data

Figure 15 shows that the seismic anomaly identified on the P(H1,V) section at site 2 is correlative with high-surface-gas concentrations. Values in parts per billion by volume (ppbv) measured at each station have been normalized by dividing them by the maximum value obtained along the transect so the different alkane concentrations can be compared between them more easily. The largest concentration peak includes high concentrations of methane (C1), ethane (C2), propane (C3), and butane (C4) recorded more than three consecutive stations or a 51 m long spread. This peak corresponds in the subsurface to blanked seismic amplitudes over a distance of approximately 130 m. Other smaller peaks are also observed along the segment sampled. Smaller gas peaks seem correlative to anomalous amplitudes on the S(H1,V) section. However, when they are compared with the large peak discussed just above, these smaller peaks do not systematically include high C1, C2, C3, and C4 values as it is the case for the main peak occurring at 250 m; this makes them less convincing candidates for potential hydrocarbon indicators. Furthermore, it points toward the fact that low gas concentrations are likely to induce amplitude anomalies.

Different markers were used to determine if thermogenic and/or biogenic processes lead to gas formation: the saturated hydrocarbon fraction (C2 + C3 + C4/C1 + C2 + C3 + C4) and ratios among C1/C2 + C3, C2/C2H4

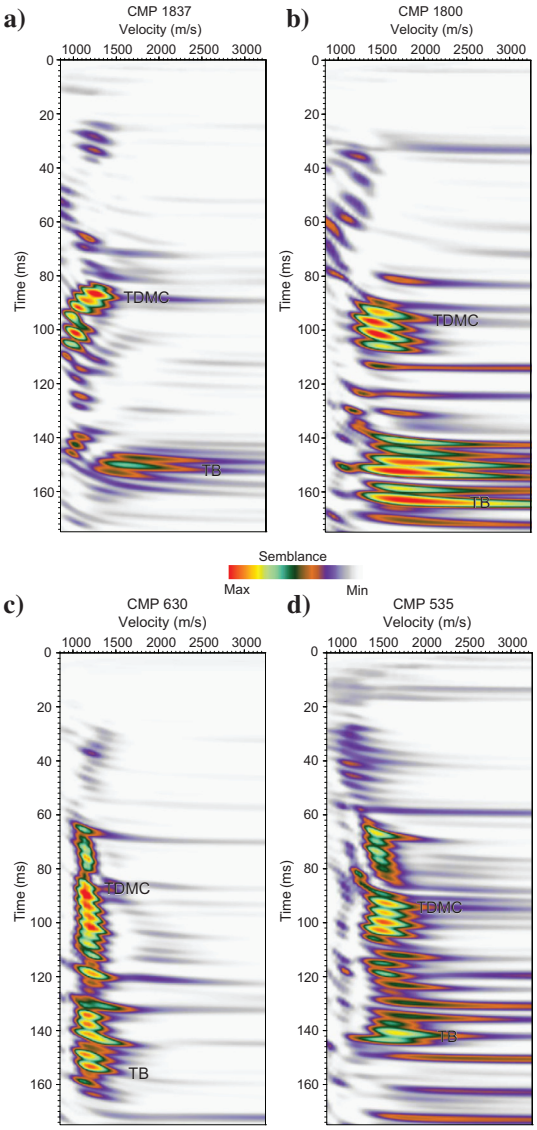

Figure 9. Semblance-based P(H1,V) velocity analyses. At site 1 (a) within the blanked zone and (b) right of it (CMP 1800) and at site 2 (c) within the pulled-down high-amplitude reflection package (CMP 630) and (d) right of it (CMP 535). See Figures 6 and 7 for CMPs location and Figure 11 for velocity picks.

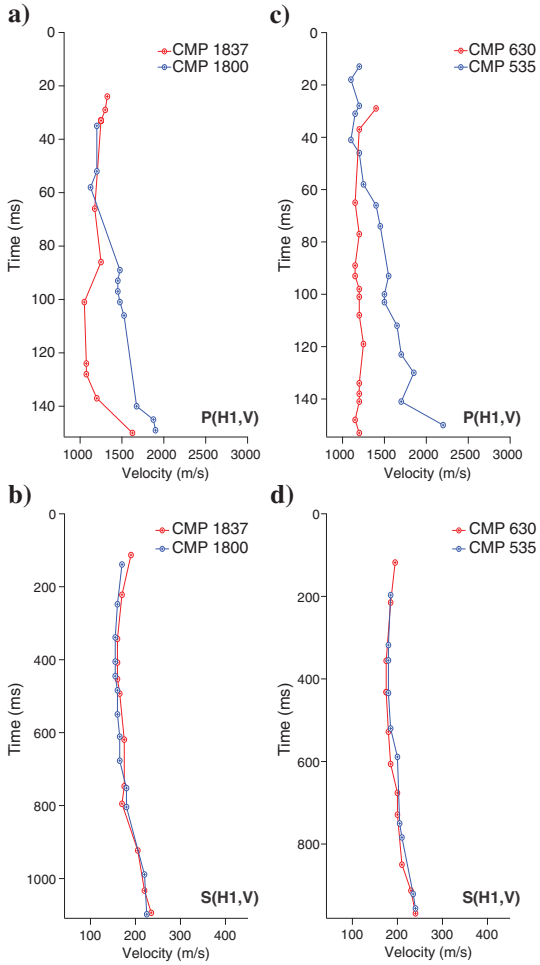

Figure 10. Semblance-based velocity picks. (a) P(H1,V) and (b) S(H1,V) picks for site 1 within the blanked zone (CMP 1837) and right of it (CMP 1800), (c) P(H1,V) and (d) S(H1, V) picks for site 2 within the pulled-down high-amplitude reflection package (CMP 630) and right of it (CMP 535). See Figures 6 and 7 for CMP locations.

(ethene), and C3/C3H6 (propene) (Table 2). Saturated fraction results show that 91% of the values falls greater than 0.05, a threshold above which gas samples are considered of thermogenic origin (Pixler, 1969). In total, 91% of the C1/C2 + C3 ratios are inferior to 50, the limit beneath which hydrocarbons are identified as being formed by thermogenic processes (Bernard, 1978). For the C2/C2H4 ratio, 97% of the stations are superior to one the value above which a thermogenic origin is given to hydrocarbons. Finally, 91% of the sampling stations have a C3/C3H6 ratio that is greater than one, the threshold above which samples are associated with a thermogenic origin. In summary, all calculated saturated and unsaturated hydrocarbon ratios indicate a thermogenic origin for gaseous fluids collected at most of the sampling stations.

Discussion

As opposed to near-surface P-wave land seismic surveys, their offshore equivalents are frequently used as front-line hydrocarbon exploration to delineate prospective areas of frontier basins in a cost-effective manner (Rollet et al., 2006; Judd and Hovland, 2007; Naudts et al., 2008; Pinet et al., 2008). Several reasons can be cited to explain the restricted use of onshore near-surface seismic data to detect active petroleum systems, e.g., heavy land use (farming, urban, and industrial areas); remote locations involving considerable costs related to equipment mobilization; the limited number or the absence of passable roads and dense forest cover that necessitate tree cutting, tree stump removal, and road construction; not to mention the large number of permits required (i.e., for land and road access, radio use, tree cutting, and the survey itself). However, the geologic knowledge available is generally much more detailed onshore than offshore because ground truth can be achieved more easily. This can benefit more targeted and strategic survey planning over areas that possess hydrocarbon-prone geologic conditions. In addition, near-surface pure S-wave surveys are easier and cheaper to conduct on land than at sea (Vanneste et al., 2011). Moreover, SH vibrators produce P-waves simultaneously. Field results presented in this paper show that the combined use of P- and S-waves provide an indirect argument to document the prospectivity of petroleum systems. However, amplitude anomalies are not always correlative to changes in subsurface geology and pore fluid content because they can also be caused by acquisition and processing inadequacies (Nanda, 2016). Of particular interest to shallow subsurface seismic imaging, are amplitude anomalies resulting from highly variable near-surface geologic conditions that impact source and receivers coupling with the ground and thus induce static effects. For the case study discussed herein, bad or a change in the source and receiver coupling with the ground is discarded because acquisition was carried out on a paved road.

Changes in type of P-amplitude anomalies caused by hydrocarbon accumulations and migration pathways

Table 1. Average 3C S-wave velocities at sites 1 and 2 and between CMPs 1550 and 1650 for the unconsolidated sediments, the top of the bedrock, and the top of the distal marine clays.

Velocity (m/s)	Site 1	Site 2	CMPs 1550–1650
Unconsolidated sediments			
S(H1,V)	159	186	154
S(H1,H1)	163	191	154
S(H1,H2)	170	191	163
Top of the bedrock			
S(H1,V)	255	245	220
S(H1,H1)	260	245	290
S(H1,H2)	255	250	260
Top of the distal marine clays			
S(H1,V)	175	190	161
S(H1,H1)	175	190	169
S(H1,H2)	170	195	177

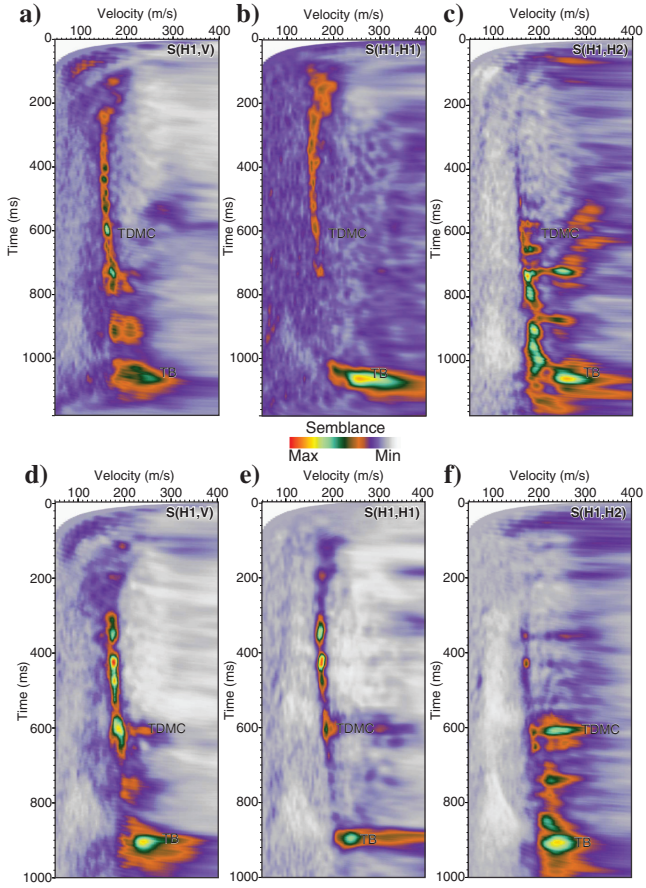

Figure 11. Three-component semblance-based S-wave velocity analyses for sites 1 (a-c) and 2 (d-f). See Figure 6 for sites 1 and 2 location and Figure 11 for velocity picks.

are frequency dependent (Kamei et al., 2004; Wood et al., 2008; Duchesne et al., 2011). Also, as gas saturation increases, wavefront propagation is affected accordingly and thus time and amplitude anomalies associated with shallow hydrocarbon accumulations present different characteristics. O'Brien (2004) mentions that seismic amplitudes are a good indication of gas occurrence but a poor indication of gas saturation. At site 1, the reflection delimiting the bedrock from the unconsolidated sediments on the P(H1,V) section shows a blanked zone in which amplitudes are abruptly diminished, whereas the same interface imaged on the S (H1,V), S(H1,H1), and S(H1,H2) sections maintains a bright character. At site 2, a blanked zone bordered by two packages of high amplitude pulled down on the P(H1,V) section, whereas S-wave data show anomalous amplitudes. S-waves are not affected by fluids as P-waves are. Therefore, this most likely explains the absence of blanking on S-wave data as opposed to their P-wave counterpart at site 1. Local and sudden amplitude blanking observed at both sites denotes that energy was scattered as opposed to being reflected probably due to the presence of gas. Shallow gas occurrence is suggested by slow P-wave velocities observed within the anomalous regions and confirmed at site 2 by surface-gas analysis. Gas is believed to vent through the fractured Utica Shale that form the top of the bedrock in the surveyed area and migrate upward into the unconsolidated sedimentary column. Hydrocarbon fraction of the sampled gas is similar to gas analyses made on Utica Shale drill cores and cuttings by Chatellier et al. (2013) and Lavoie et al. (2016). This most likely explains the abrupt amplitude blanking of the bedrock reflection at site 1 and the decrease in amplitude for the same marker and the blanked zone imaged between 20 and 50 ms both documented at site 2 on the P(H1,V) data.

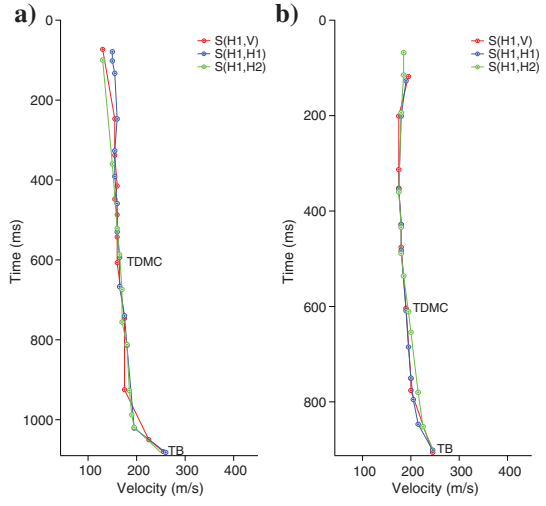

Figure 12. S(H1,V), S(H1,H1), and S(H1,H2) semblance-based velocity picks for (a) site 1 and (b) site 2. See Figure 6 for both sites' locations.

Low and high gas saturation tends to produce pull downs and amplitude enhancements because low saturation affects P-wave velocity and amplitude as much as high saturation does (Hilterman, 2001; Han and Batzle, 2002; O'Brien 2004; Navalpakam et al., 2012). Therefore, the high-amplitude pull-down reflection packages observed at site 2 could indicate unconsolidated sediments with low or high gas saturation. For scattering to cause important amplitude blanking such as what is observed in this study, one could think that total gas saturation must be reached. However, the relationship between the amount of scattering and gas saturation is not linear. Landmark work of White (1975) initially portrayed the relationship between partial or patchy gas saturation with significant attenuation. According to the author, attenuation results from fluid flow induced by pore pressure differences located at boundaries in which change of fluid phase occurs. White's model was revisited and refined by several other studies (Dutta and Odé, 1979; Mavko and Mukerji, 1998; Rubino and Holliger, 2012) being mostly discussed in terms of seismic attenuation and velocity dispersion. Poroelastic numerical experiments of wave propagation in White's partially saturated model conducted by Carcione et al. (2003) showed that large attenuation is due to increased dissipation that is in turn caused by scattering and conversion from fast to slow P-wave. The upward migration of partially gas-saturated groundwater is suggested as being the cause for important P-amplitude blanking observed in this study. This could also explain the correlation between the largest peak of hydrocarbon concentration with blanked P-amplitude at site 2 (Figure 15).

Anomalously high amplitudes noticed at site 2 on S-wave data are more puzzling. Comparable lateral amplitude variations have been observed approximately 75 km south-southeast from the study site by Pugin et al. (2013a) in a similar geologic context. They were interpreted as depositional layering of the muds disrupted by vertical fluid migration. Cheel and Rust

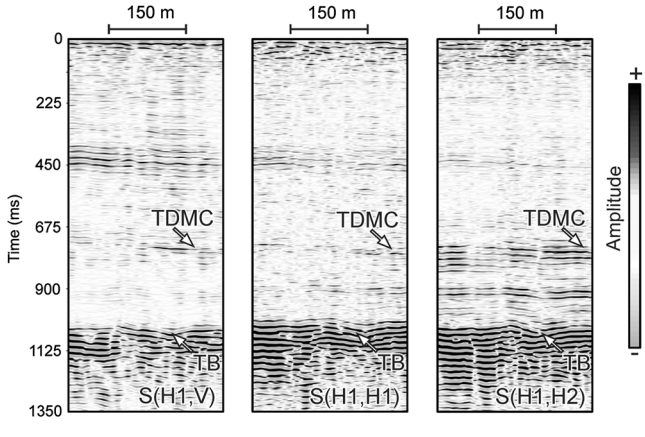

Figure 13. S(H1,V), S(H1,H1), and S(H1,H2) sections at the comparison site. TDMC, top of distal marine clays; TB, top of bedrock; and BZ, blanked zone. See Figure 6 for comparison site location.

(1986) describe disturbed unconsolidated sediment layers exposed more than 10 m thick sections in sands and gravel pits in the Ottawa region located approximately 250 km southwest of the investigated area. They claim that soft sediment deformation causing bedding disruption is the result of excessive pore water pressure. Despite that the pore pressure increase is attributed to slumping on subaqueous fans and/or to the meltout of ice blocks that had been buried by glacial sediments in this case, similar structures can be formed by different loading mechanisms. For example, the upward migration of overpressured gas coming from a deeper source that is mixing up with pore water contained in unconsolidated deposits can cause sediment layer breakage (Sherry et al., 2012). Although they have not been extensively reported in the literature, overpressured zones associated with shallow gas occurrences are frequently encountered during geotechnical and hydrogeological well drilling in the St. Lawrence Lowlands (D. Perret, personal communication, 2015). The most mediatized incident occurred in Quebec City in the fall of 2014 when drillers hit a shallow thermogenic gas pocket perched in unconsolidated sediments at a depth of 60 m while implanting a geotechnical well. In this study, based on the thermogenic signature proposed by the surface-gas analysis, gas source is believed to be Utica Shale that extends from the top of the bedrock to approximately 340 m down below (Bédard et al., 2013; Rivard et al., 2014). As hydrocarbon-rich fluids migrate into unconsolidated sediments they tend to modify porosity, grain alignment, and density (Li and Pyrak-Nolte, 1998; Lavoie et al., 2010; Vanorio, 2015). Lavoie et al. (2010) observe carbonate cement precipitation in unconsolidated marine sediments from material sampled within an active hydrocarbon vent located in the St. Lawrence Estuary (Eastern Canada). This ultimately impacts the seismic signature of geologic media. It is proposed that amplitude anomalies observed on S-wave data are probably due to local changes in the physical properties (e.g., density, porosity) of the matrix induced by vertical fluid migration. Lavoie et al. (2010) observe carbonate cement precipitation in unconsoli-

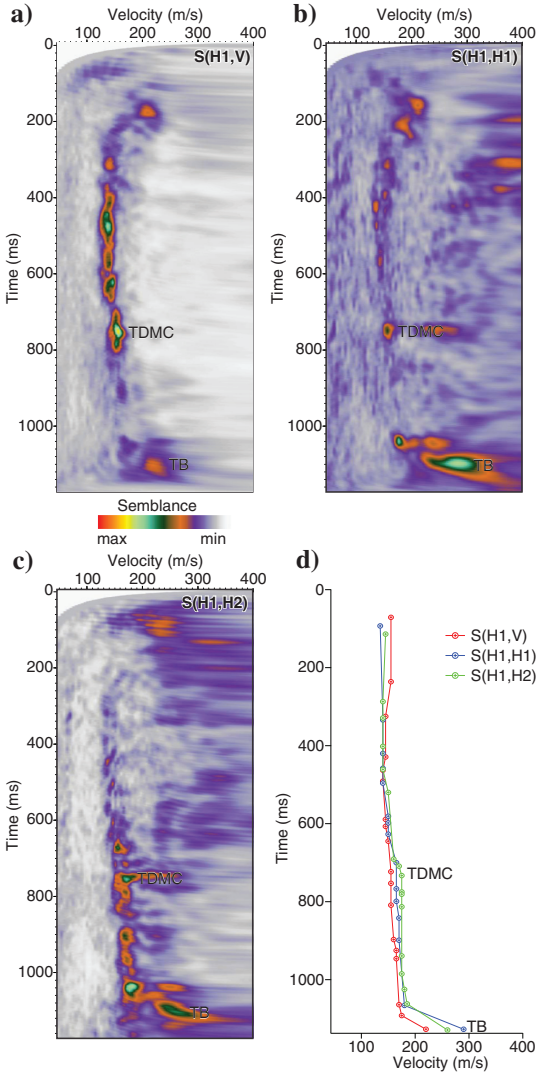

Figure 14. Semblance-based S-wave velocity analyses made for (a) V, (b and c) H1 and H2-receiver components between CMPs 1500 and 1650. (d) Semblance-based velocity picks of all 3C. See Figure 6 for CMP locations.

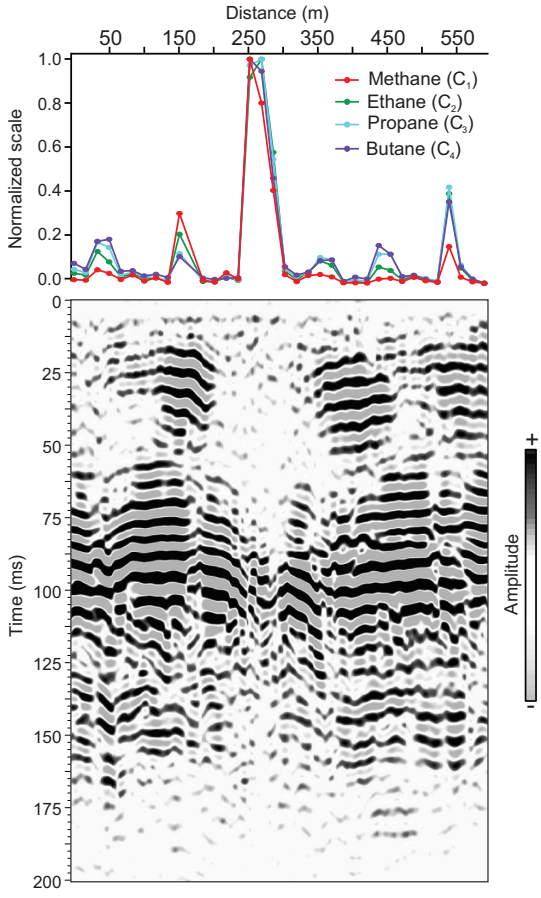

Figure 15. Correlation between surface-gas analysis and P (H1,V) section at site 2. See Figure 6 for location.

dated marine sediments from material sampled within an active hydrocarbon vent located in the St. Lawrence Estuary. This ultimately impacts the seismic signature of geologic media. It is proposed that amplitude anomalies observed on S-wave data are probably due to local changes in the physical properties (e.g., density, porosity) of the matrix induced by vertical fluid migration.

Sites 1 and 2 do not present any signs of a directional change in velocity or seismic anisotropy (Figures 11 and 12; Table 1). However, between CMPs 1550 and 1650, i.e., a part of the seismic line where no upward fluid migration is suspected to happen, S(H1,H2) velocity can be up to 11% faster than S(H1,V) velocity at the top of the distal marine clays supporting a vertical transverse isotropy (VTI) (Thomsen, 1986; Figure 13d). This is comparable to the 15% difference between S(H1, H2) and S(H1,V) velocities reported by Pugin et al. (2013b) in similar geologic conditions. These authors have also observed that reflections sitting just above the top of the bedrock are better imaged on the H2-component of the receiver stations. In this study, a similar signature is observed on the same component for the same events. For both sites, between the free surface and the top of the distal marine, S-wave data show higher energy recorded on the vertical component than on the horizontal components. However, no significant directional change in amplitude or polarization is noticed on any components at the comparison site (Figure 13). Although, a detailed polarization and anisotropy analysis is beyond the scope of this paper, a relationship between the vertical polarization of the seismic energy and the occurrence of hydrocarbon seeps can be postulated. Local perturbations of the matrix can be induced by fluid migration. This can punctually alter the vertically transverse isotropic background documented in the St. Lawrence Lowlands, influencing S-wave polarization along the way (Pugin et al., 2009, 2013a; Blouin, 2015; Figure 16). However, this hypothesis remains to be tested using an acquisition geometry that is optimal to capture high-quality polarization and anisotropy indicators at shallow depth (>10 m) as a very short distance between the source and the first offset and closer receiver spacing are needed. Moreover, Alford rotation could be explored so the direction of propagation of fast and slow S-wave is better circumscribed (Alford, 1986).

Table 2. Hydrocarbon ratios obtained from surface-gas sampling stations.

Station number	Saturated fraction	C3/ C3H6	C2/ C2H4	C1/C2 + C3
YM-001	0.166	2.343	3.739	11.667
YM-002	0.153	1.007	1.459	7.866
YM-003	0.148	8.31	12.231	18.591
YM-004	0.149	10.366	13.856	16.859
YM-005	0.112	1.508	1.965	13.692
YM-006	0.076	2.499	4.542	31.504
YM-007	0.132	1.915	2.989	13.667
YM-008	0.067	1.786	4.054	36.137
YM-009	0.111	0.678	0.989	9.084
YM-011	0.042	2.202	6.706	84.172
YM-012	0.054	0.939	2.64	35.308
YM-013	0.087	1.088	2.114	18.408
YM-014	0.042	1.084	2.012	38.178
YM-015	0.05	1.029	2.302	37.011
YM-016	0.062	10.651	15.146	56.446
YM-017	0.08	13.63	21.827	46.344
YM-018	0.088	11.814	20.609	42.549
YM-019	0.093	2.681	4.389	25.13
YM-020	0.136	3.524	3.871	13.783
YM-021	0.087	1.076	1.832	17.502
YM-022	0.15	2.866	4.425	14.268
YM-023	0.168	4.721	7.068	14.065
YM-024	0.093	3.624	N/A	35.929
YM-025	0.141	1.55	2.094	10.821
YM-026	0.131	1.345	1.881	11.143
YM-027	0.23	18.848	16.929	9.863
YM-028	0.182	3.216	3.558	8.826
YM-029	0.123	1.158	1.414	9.726
YM-030	0.083	1.361	2.522	21.939
YM-031	0.104	1.17	2.079	14.9
YM-032	0.101	1.023	1.675	13.301
YM-033	0.146	15.609	25.253	22.8
YM-034	0.146	7.811	21.708	21.249
YM-035	0.124	3.574	9.646	21.219
YM-036	0.045	5.378	2.969	36.352

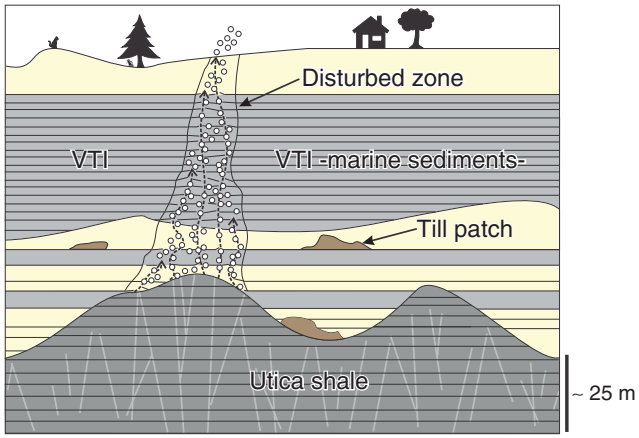

Figure 16. Sketch showing how hydrocarbons migrate from the fractured Utica Shale toward the surface through Quaternary deposits. Elastic properties of unconsolidated marine sediments (VTI medium) are altered as porosity, grain alignment, density, and layering are disturbed by upward fluid movements.

Conclusions

Because P-waves are sensitive to fluids and S-waves are not, the simultaneous acquisition of P- and S-wave seismic reflection data is attractive to constrain the nature of potential near-surface hydrocarbon indicators. Two examples located in a prospective area of the St. Lawrence Lowlands in Eastern Canada were presented to demonstrate the effectiveness of such a method. For both sites, P-wave data show local changes in reflection amplitude and slow velocities, whereas S-wave data present anomalous amplitude at one site. Differences between the morphology and the amplitude of P- and S-wave reflections as well as the abrupt decrease in P-velocity are indirect lines of evidence for hydrocarbon migration toward the surface through unconsolidated sediments. Surface-gas analysis made on samples taken at one site reveals the occurrence of thermogenic gas that presumably vents from the underlying fractured Utica shales forming the top of the bedrock. The 3C shear data suggest that fluid migration locally disturbs the elastic properties of the matrix.

Finally, this seismic method is not restricted to shallow hydrocarbon prospection as it can also help to circumscribe hazardous areas for drilling, contribute to baseline studies for groundwater quality control and support the quantification of methane fluxes into the atmosphere.

Acknowledgments

The authors would like to thank S. Pullan, T. Cartwright, K. Brewer, and M. Douma (all from the Near-Surface Geophysics Section of the Geological Survey of Canada) for field work support during seismic acquisition. Intragaz is also acknowledged for providing access to borehole information. B. Dietiker (GSC-Ottawa) kindly reviewed the initial version of the manuscript. The authors are indebted to D. Perret (GSC-Quebec) for fruitful discussions about the elastic characteristics of the St. Lawrence Lowlands' near surface. Three anonymous reviewers are acknowledged for their constructive comments that helped to improve the quality of the document. This work was supported by the Groundwater Geoscience and Environmental Geoscience programs of the Geological Survey of Canada. This is GSC contribution no. 20150352.

References

Alford, R. M., 1986, Shear data in the presence of azimuthal anisotropy: Dilley, Texas: 56th Annual International Meeting, SEG, Expanded Abstracts, 476–479.

Batzle, M., and Z. Wang, 1992, Seismic properties of pore fluids: Geophysics, **57**, 1396–1408, doi: 10.1190/1.1443207.

Bédard, K., M. Malo, and F.-A. Comeau, 2013, CO_2 geological storage in the Province of Québec, Canada — Capacity evaluation of the St. Lawrence Lowlands basin: Energy Procedia, **37**, 5093–5100, doi: 10.1016/j.egypro.2013.06.422.

Bernard, B., 1978, Light hydrocarbons in marine sediments: Ph.D. thesis, Texas A&M University.

Blouin, M., 2015, Assimilation de données géophysiques pour la caractérisation hydrogéologique régionale: Optimisation de la séquence: Ph.D. thesis, Institut National de la Recherche Scientifique, Centre Eau Terre Environnement.

Carcione, J. M., H. B. Helle, and N. H. Pham, 2003, White's model for wave propagation in partially saturated rocks: Comparison with poroelastic numerical experiments: Geophysics, **68**, 1389–1398, doi: 10.1190/1.1598132.

Chatellier, J. Y., K. Ferworn, N. L. Larsen, S. Ko, P. Flek, M. Molgat, and I. Anderson, 2013, Overpressure in shale gas: When geochemistry and reservoir engineering data meet and agree, *in* J. Y. Chatellier, and D. Jarvie, eds., Critical assessment of shale gas resource play: AAPG Memoir 103, 45–69.

Cheel, R. J., and B. R. Rust, 1986, A sequence of soft-sediment deformation (dewatering) structures in Late Quaternary subaqueous outwash near Ottawa, Canada: Sedimentary Geology, **47**, 77–93, doi: 10.1016/0037-0738(86)90072-2.

Cherry, J., 1962, The azimuthal and polar radiation patterns obtained from a horizontal stress applied at the surface of an elastic half space: Bulletin of the Seismological Society of America, **52**, 27–36.

Chiu, S. K., and P. Butler, 1997, 2D/3D coherent noise attenuation by locally adaptive modeling and removal on prestack data: 67th Annual International Meeting, SEG, Expanded Abstracts, 1309–1311.

Chopra, S., and K. J. Marfurt, 2007, Seismic attributes for prospect identification and reservoir characterization: SEG.

Clark, J. C., W. J. Johnson, and W. A. Miller, 1994, The application of high resolution shear wave seismic reflection surveying to hydrogeological and geotechnical investigations: 7th Annual Symposium, EEGS-SAGEEP, Extended Abstracts, 231–245.

Clet, M., and S. Occhietti, 1996, La sous-séquence des sédiments de Saint-Pierre — Rythmites du Saint-Maurice — Sables des Vieilles-Forges, Pléistocène supérieur, vallée du Saint-Laurent, Québec: Géographie Physique et Quaternaire, **50**, 287–310, doi: 10.7202/033101ar.

Coruh, C., and J. K. Costain, 1983, Noise attenuation by vibroseis whitening (VSW) processing: Geophysics, **48**, 543–554, doi: 10.1190/1.1441485.

Crampin, S., 1985, Evaluation of anisotropy by shear-wave splitting: Geophysics, **50**, 142–152, doi: 10.1190/1.1441824.

Dai, H., X.-Y. Li, and P. Conway, 2007, Imaging beneath gas clouds using 3D prestack Kirchhoff time migration of PS-converted waves — A case study from the North Sea: The Leading Edge, **26**, 522–529, doi: 10.1190/1.2723216.

Dasios, A., C. McCann, T. R. Astin, D. M. McCann, and P. Fenning, 1999, Seismic imaging of the shallow subsurface: Shear wave case histories: Geophysical Prospecting, **47**, 565–591, doi: 10.1046/j.1365-2478.1999.00138.x.

Duchesne, M. J., E. J. Halliday, and J. V. Barrie, 2011, Analyzing seismic imagery in the time-amplitude and time-frequency domains to determine fluid nature and migration pathways: A case study from the Queen Charlotte Basin, offshore British Columbia: Journal of Applied Geophysics, **73**, 111–120, doi: 10.1016/j.jappgeo.2010.12.002.

Duchesne, M. J., and A. J. M. Pugin, 2014, Analysis of P-wave and S-wave data on near-surface potential hydrocarbon indicators: Presented at the EAGE Shallow Anomalies Workshop: Indications of Prospective Petroleum Systems?.

Dutta, N. C., and H. Odé, 1979, Attenuation and dispersion of compressional waves in fluid filled porous rocks with partial gas saturation (White model) — Part II: Results: Geophysics, **44**, 1789–1805, doi: 10.1190/1.1440939.

Ensley, R. A., 1984, Comparison of P- and S-wave seismic data: A new method for detecting gas reservoirs: Geophysics, **49**, 1420–1431, doi: 10.1190/1.1441771.

Gaiser, J., and A. Strudley, 2005, Acquisition and application of multicomponent vector wavefields: Are they practical?: First Break, **23**, 61–67, doi: 10.3997/1365-2397.2005012.

Gao, L., J. Xia, and Y. Pan, 2014, Misidentification caused by leaky surface wave in high-frequency surface wave method: Geophysical Journal International, **199**, 1452–1462, doi: 10.1093/gji/ggu337.

Ghose, R., and J. Goudswaard, 2004, Integrating S-wave seismic-reflection data and cone-penetration-test data using a multiangle multiscale approach: Geophysics, **69**, 440–459, doi: 10.1190/1.1707064.

Han, D.-H., and M. Batzle, 2002, Fizz water and low gas-saturated reservoirs: The Leading Edge, **21**, 395–398, doi: 10.1190/1.1471605.

Hardage, B. A., and D. Wagner, 2014a, Generating direct-S modes with simple, low-cost, widely available seismic sources: Interpretation, **2**, no. 2, SE1–SE15, doi: 10.1190/INT-2013-0095.1.

Hardage, B. A., and D. Wagner, 2014b, S-S imaging with vertical-force sources: Interpretation, **2**, no. 2, SE29–SE38, doi: 10.1190/INT-2013-0097.1.

Hilterman, F., 2001, Seismic amplitude interpretation: SEG/EAGE.

Intragaz, 2009, Pointe-du-Lac Site, http://www.intragaz.com/en/activities_pdl.html, accessed 9 October 2014.

Jones, I. F., and S. Levy, 1987, Signal-to-noise ratio enhancement in multichannel seismic data via the Karhunen-Loéve Transform: Geophysical Prospecting, **35**, 12–32, doi: 10.1111/gpr.1987.35.issue-1.

Judd, A., and M. Hovland, 2007, Seabed fluid flow the impact on geology, biology and the marine Environment: Cambridge University Press.

Kamei, R., M. Hato, and T. Matsuoka, 2004, Random heterogeneous model with bi-modal velocity distribution — Application to methane hydrate-bearing zone: Proceedings of the 7th SEGJ International Symposium, 66–71.

Lamb, H., 1904, On the propagation of tremors over the surface of an elastic solid: Philosophical Transactions of the Royal Society A: Mathematical, Physical and Engineering Sciences, **203**, 1–42, doi: 10.1098/rsta.1904.0013.

Lamothe, M., 1989, A new framework for the Pleistocene stratigraphy of the central St. Lawrence Lowland, Southern Quebec: Géographie Physique et Quaternaire, **43**, 119–129, doi: 10.7202/032764ar.

Larner, K. L., E. J. Mateker, Jr., and C. S. Wu, 1974, New interest in an old friend: Oil and Gas Journal, **72**, 70–78.

Lavoie, D., N. Pinet, G. Bordeleau, O. H. Ardakani, P. Ladevèze, M. J. Duchesne, C. Rivard, A. Mort, V. Brake, H. Sanei, and X. Malet, 2016, The Upper Ordovician black shales of southern Quebec (Canada) and their significance for naturally occurring hydrocarbons in shallow groundwater: International Journal of Coal Geology, **158**, 44–64, doi: 10.1016/j.coal.2016.02.008.

Lavoie, D., N. Pinet, J. Dietrich, P. Hannigan, S. Castonguay, T. Hamblin, and P. Giles, 2009, Petroleum resource assessment, paleozoic successions of the St. Lawrence platform and Appalachians of eastern Canada: Open File 6174, Geological Survey of Canada.

Lavoie, D., N. Pinet, M. J. Duchesne, A. Bolduc, and R. Larocque, 2010, Methane-derived authigenic carbonates from active hydrocarbon seeps of the St. Lawrence Estuary, Canada: Marine and Petroleum Geology, **27**, 1262–1272, doi: 10.1016/j.marpetgeo.2010.02.014.

Leblanc, Y., G. Légaré, K. Lacasse, M. Parent, and S. Campeau, 2013, Caractérisation hydrogéologique du sud-ouest de la Mauricie. Rapport déposé au ministère du Développement durable, de l'Environnement, de la Faune et des Parcs dans le cadre du Programme d'acquisition de connaissances sur les eaux souterraines du Québec: Département des sciences de l'environnement, Université du Québec à Trois-Rivières.

Li, X., and L. J. Pyrak-Nolte, 1998, Acoustic monitoring of sediment-pore fluid interaction: Geophysical Research Letters, **25**, 3899–3902, doi: 10.1029/1998GL900028.

Maercklin, N., and A. Zollo, 2009, Estimation of elastic contrasts in a layered model from seismic PS-to-PP amplitude ratios: Geophysical Journal International, **179**, 1617–1626, doi: 10.1111/gji.2009.179.issue-3.

Mavko, G., and T. Mukerji, 1998, Bounds on low-frequency seismic velocities in partially saturated rocks: Geophysics, **63**, 918–924, doi: 10.1190/1.1444402.

McCormack, M. D., J. A. Dunbar, and W. W. Sharp, 1984, A case study of stratigraphic interpretation using shear and compressional seismic data: Geophysics, **49**, 509–520, doi: 10.1190/1.1441686.

Miller, G. F., and H. Pursey, 1954, The field and radiation impedance of mechanical radiators on the free surface of a semi-infinite isotropic solid: Proceedings of the Royal Society A: Mathematical, Physical and Engineering Sciences, **223**, 521–541.

Nanda, N. C., 2016, Seismic data interpretation and evaluation for hydrocarbon exploration and production: A practitioner's guide: Springer.

Naudts, L., J. Greinert, Y. Artemov, S. E. Beaubien, C. Borowski, and M. de Batist, 2008, Anomalous sea-floor backscatter patterns in methane venting areas, Dnepr paleo-delta, NW Black Sea: Marine Geology, **251**, 253–267, doi: 10.1016/j.margeo.2008.03.002.

Navalpakam, R. S., I. A. Pecher, and T. Stern, 2012, Weak and segmented bottom simulating reflections on the Hikurangi Margin, New Zealand — Implications for gas hydrate reservoir rocks: Journal of Petroleum Science and Engineering, **88–89**, 29–40, doi: 10.1016/j.petrol.2012.01.008.

O'Brien, J., 2004, Seismic amplitudes from low gas saturation sands: The Leading Edge, **23**, 1239–1243.

Pinet, N., M. J. Duchesne, D. Lavoie, A. Bolduc, and B. Long, 2008, Surface and subsurface signatures of gas seepage in the St. Lawrence Estuary (Canada): Significance to hydrocarbon exploration: Marine and Petroleum Geology, **25**, 271–288, doi: 10.1016/j.marpetgeo.2007.07.011.

Pixler, B. O., 1969, Formation evaluation by analysis of hydrocarbon ratios: Journal of Petroleum Technology, **21**, 665–670, doi: 10.2118/2254-PA.

Pugin, A. J. M., K. Brewer, T. Cartwright, S. E. Pullan, D. Perret, H. Crow, and J. A. Hunter, 2013a, Near surface S-wave seismic reflection profiling — New approaches and insights: First Break, **31**, 49–60, doi: 10.3997/1365-2397.2013005.

Pugin, A. J. M., S. E. Pullan, and M. J. Duchesne, 2013b, Regional hydrostratigraphy and insights into fluid flow through a clay aquitard from shallow seismic reflection data: The Leading Edge, **32**, 742–748, doi: 10.1190/tle32070742.1.

Pugin, A. J. M., S. E. Pullan, and J. A. Hunter, 2009, Multicomponent high-resolution seismic reflection profiling: The Leading Edge, **28**, 1248–1261, doi: 10.1190/1.3249782.

Rivard, C., D. Lavoie, R. Lefebvre, S. Séjourné, C. Lamontagne, and M. J. Duchesne, 2014, An overview of Canadian shale gas production and environmental concerns: International Journal of Coal Geology, **126**, 64–76, doi: 10.1016/j.coal.2013.12.004.

Robertson, J. D., and W. C. Pritchett, 1985, Direct hydrocarbon detection using comparative P-wave and S-wave seismic sections: Geophysics, **50**, 383–393, doi: 10.1190/1.1441918.

Rollet, N., G. A. Logan, J. M. Kennard, P. E. O'Brien, A. T. Jones, and M. Sexton, 2006, Characterisation and correlation of active hydrocarbon seepage using geophysical data sets: An example from the tropical, carbonate Yampi Shelf, Northwest Australia: Marine and Petroleum Geology, **23**, 145–164, doi: 10.1016/j.marpetgeo.2005.10.002.

Roth, M., and K. Holliger, 2000, The non-geometric PS wave in high-resolution seismic data: Observations and modelling: Geophysical Journal International, **140**, F5–F11, doi: 10.1046/j.1365-246x.2000.00030.x.

Rubino, G., and K. Holliger, 2012, Seismic attenuation and velocity dispersion in heterogeneous partially saturated porous rocks: Geophysical Journal International, **188**, 1088–1102, doi: 10.1111/gji.2012.188.issue-3.

Sheriff, R. E., and L. P. Geldart, 1995, Exploration seismology: Cambridge University Press.

Sherry, T. J., C. D. Rowe, J. D. Kirkpatrick, and E. E. Brodsky, 2012, Emplacement and dewatering of the world's largest exposed sand injectite complex: Geochemistry, Geophysics and Geosystems, **13**, 1–17.

Simm, R., and M. Bacon, 2014, Seismic amplitude: An interpreter's handbook: Cambridge University Press.

St-Antoine, P., and Y. Héroux, 1993, Genèse du gaz naturel de la région de Trois-Rivières, basses terres du Saint-Laurent et de Saint-Flavien, Appalaches, Québec, Canada: Canadian Journal of Earth Sciences, **30**, 1881–1885, doi: 10.1139/e93-166.

Stewart, R. R., J. E. Gaiser, J. Brown, and D. C. Lawton, 2002, Converted-wave seismic exploration: Methods: Geophysics, **67**, 1348–1363, doi: 10.1190/1.1512781.

Taner, M. T., F. Koehler, and R. E. Sheriff, 1979, Complex seismic trace analysis: Geophysics, **44**, 1041–1063, doi: 10.1190/1.1440994.

Taylor, O.-D. S., M. H. McKenna, M. C. L. Quinn, and B. G. Quinn, 2014, Partially saturated soil causing significant variability in near surface seismic signals: Near Surface Geophysics, **12**, 467–480, doi: 10.3997/1873-0604.2013039.

Thomsen, L., 1986, Weak elastic anisotropy: Geophysics, **51**, 1954–1966, doi: 10.1190/1.1442051.

Vanneste, M., C. Madshus, V. L. Socco, M. Maraschini, P. M. Sparrevik, H. Westerdahl, K. Duffau, E. Skomedal, and T. I. Bjørnar, 2011, On the use of the Norwegian Geotechnical Institute's prototype seabed-coupled shear wave vibrator for shallow soil characterization — I. Acquisition and processing of multimodal surface waves: Geophysical Journal International, **185**, 221–236, doi: 10.1111/j.1365-246X.2011.04960.x.

Vanorio, T., 2015, Recent advances in time-lapse, laboratory rock physics for the characterization and monitoring of fluid-rock interactions: Geophysics, **80**, no. 2, WA49–WA59, doi: 10.1190/geo2014-0202.1.

van der Kolk, C. M., W. S. Guest, and J. H. H. M. Potters, 2001, The 3D shear experiment over the Natih field in Oman: The effect of fracture-filling fluids on shear propagation: Geophysical Prospecting, **49**, 179–197, doi: 10.1046/j.1365-2478.2001.00250.x.

White, J. E., 1975, Computed seismic speeds and attenuation in rocks with partial gas saturation: Geophysics, **40**, 224–232, doi: 10.1190/1.1440520.

Wiest, B., and H. A. K. Edelmann, 1984, Static corrections for shear wave sections: Geophysical Prospecting, **32**, 1091–1102, doi: 10.1111/gpr.1984.32.issue-6.

Wood, W. T., P. E. Hart, D. R. Hutchinson, N. Dutta, F. Snyder, R. B. Coffin, and J. F. Gettrust, 2008, Gas and gas hydrate distribution around seafloor seeps in Mississippi Canyon, Northern Gulf of Mexico, using multi-resolution seismic imagery: Marine and Petroleum Geology, **25**, 952–959, doi: 10.1016/j.marpetgeo.2008.01.015.

Woolery, E. W., R. L. Street, Z. Wang, and J. B. Harris, 1993, Near-surface deformation in the New Madrid seismic zone as imaged by high resolution SH-wave seismic methods: Geophysical Research Letters, **20**, 1615–1618, doi: 10.1029/93GL01658.

Xue, Y.-J., J.-X. Cao, D.-X. Wang, R.-F. Tian, and Y.-X. Shua, 2013, Detection of gas and water using HHT by analyzing P- and S-wave attenuation in tight sandstone gas reservoirs: Journal of Applied Geophysics, **98**, 134–143, doi: 10.1016/j.jappgeo.2013.08.023.

Mathieu J. Duchesne received a Ph. D. in geodynamics and resources from the Institut National de la Recherche Scientifique, Centre Eau-Terre-Environnement, where he is also an adjunct professor and a member of the Laboratoire d'Imagerie et d'Acquisition Géophysique. Currently, he is a researcher specializing in reflection seismology for the Geological Survey of Canada at the Quebec City office. His work focuses on the development of seismic processing algorithms and analysis of hydrocarbon indicators on seismic data.

André Pugin received a doctorate from the University of Geneva, Switzerland, in 1989. During many post docs, he has been involved in collaborative applied geophysics projects in America, Europe, and Asia for solving environmental, hydrogeological, geotechnical, and climatic problems. Since 2006, he works as a engineering and groundwater geophysicist at the Geological Survey of Canada, Ottawa. His interest in sedimentary basin architecture has driven him to test, develop, and use various geophysical techniques, including high-resolution seismic reflection using 3C landstreamers to obtain detailed images of subsurface architecture and depositional information. He is member of SEG and EAGE and fellow member of GSA.

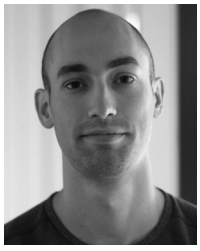

Gabriel Fabien-Ouellet is a Ph. D. student at the Institut National de la Recherche Scientifique, Centre Eau-Terre-Environnement. He is specialized in seismic processing and develops new approaches to apply full-waveform inversion to near-surface surveys.

Mathieu Sauvageau received a master's degree in earth sciences from the Institut National de la Recherche Scientifique and Centre Eau-Terre-Environnement. He is currently enrolled as a Ph.D. student in mining engineering from McGill University. He works on the valuation of companies affected by cycles in commodity markets. His project was focused on the implementation of a statistical method for improving the estimation of porosity in an oil reservoir.